Enhanced leakage current properties of Ni-doped $Ba_{0.6}Sr_{0.4}TiO_3$ thin films driven by modified band edge state

Hyungtak Seo,[1] Young-Bae Kim,[2,a)] Gerald Lucovsky,[3] Il-Doo Kim,[4] Kwun-Bum Chung,[5] Hikaru Kobayashi,[6] and Duck-Kyun Choi[7,b)]
[1]*Department of Chemistry and Materials Sciences Division, Lawrence Berkeley National Laboratory, University of California, Berkeley, California 94720, USA*
[2]*Samsung Advanced Institute of Technology, Suwon 440-600, South Korea*
[3]*Department of Physics, North Carolina State University, Raleigh, North Carolina 27695, USA*
[4]*Center for Energy Materials Research, Korea Institute of Science and Technology, P.O. Box 131, Cheongryang, Seoul 130-650, South Korea*
[5]*Department of Physics, Dankook University, Dongnamgu, Anseodong 29, Cheonan 330-714, South Korea*
[6]*Institute of Scientific and Industrial Research, Osaka University, Osaka 567-0047, Japan*
[7]*Division of Material Science and Engineering, Hanyang University, 17 Haengdang-dong, Seongdong-gu, Seoul 133-791, South Korea*

(Received 8 October 2009; accepted 12 December 2009; published online 28 January 2010)

1% Ni-doped barium strontium titanate (BST) thin film deposited at room temperature reveals the significantly enhanced leakage current performance which is extraordinarily effective for low temperature applications. Significant leakage current suppression of >2 orders was achieved for electric fields from 0.25 to 2 MV/cm in Pt/Ni-doped BST/Pt metal-insulator-metal (MIM) capacitor cells compared to undoped BST. For Ni doping at the 1% level, the spectral dependence of (i) the imaginary part of the complex dielectric constant, ε_2, obtained from the rotating compensator enhanced spectroscopic ellipsometry and (ii) OK_1 absorption spectra obtained from synchrotron x-ray absorption spectroscopy shows significant differences (0.26 ± 0.15 eV) in the conduction band edge trap depth relative to undoped BST. The valence band (VB) edge x-ray photoelectron spectroscopy analysis reveals the Fermi energy level downshift of 0.4 eV for Ni-doped BST toward the VB edge. There is a direct correlation between these changes in band edge states of BST thin films with Ni doping and the improved electrical performance in MIM capacitors led by the qualitatively different charge injection mechanism. The proposed transition metal doping process and analysis approach provide a pathway for charge injection control driven by band edge state changes in other perovskite oxides for low temperature (i.e., room temperature) applications.
 [doi:10.1063/1.3291124]

I. INTRODUCTION

Barium strontium titanate, $Ba_xSr_{1-x}TiO_3$ (x=0.3–0.7, hereafter, BST), has been investigated as a high-dielectric constant (k) material for various applications in advanced electronic devices such as storage capacitors in gigabit dynamic random-access memory, microwave tunable devices, and ferroelectric random-access memories.[1–4] In particular, there has been recent interest in the potential use of BST thin films as a gate dielectric for producing ZnO-based[5] transparent thin film transistors (TFTs) because the relatively high-dielectric constant of BST compared to other high-k oxides such as barium zirconium titanate (BZT),[6] Al_2O_3,[7,8] HfO_2,[8,9] and TiO_2 (Ref. 10) could induce the low operating voltages of ZnO TFTs. It has been widely reported that the electronic transport properties of the ZnO channels in TFTs are very susceptible to gate dielectrics because gate dielectrics affect the interfacial states, surface roughness, and gate leakage currents.[7,11–14] In addition, the thickness of high-k gate oxides should be over 200 nm when the TFTs are fabricated on rough plastic substrates to avoid the pin hole problems that are detrimental to ZnO-TFT operation.[11] Whereas the referenced TFTs that use high-k dielectrics have demonstrated promising TFT performance, most of them still show poor gate leakage current characteristics at the gate voltage bias above 5V.[5,8,9,15] This poor leakage current is closely related to the material properties of room temperature (RT)-deposited high-k dielectrics, since the gate dielectrics for transparent TFTs cannot often be annealed at high temperature due to the limited thermal stability of transparent glasses substrates. However, most complex transition metal (TM) oxide thin films including BST should be annealed at relatively high temperatures of above 300 °C to further improve the leakage current characteristics.[5,16–18]

Even for thermally annealed high-k BST, earlier studies have indicated significant reliability issues associated with BST devices.[19–23] Major problems were attributed to metal contact interfacial states when using ultrathin oxides.[19] These characteristics often induce asymmetric high current leakage under moderately high bias voltages.[21] There are other important issues associated with long-term reliability under both constant positive and negative voltage stresses.[23] For RT-deposited BST thin films with nanocrystallites in the range of a few nanometers, reliability issues such as a high leakage current and low oxide breakdown voltage are usually

a)Electronic mail: yb305.kim@samsung.com.
b)Electronic mail: duck@hanyang.ac.kr.

more critical; thus, RT-deposited BST thin films cannot be implanted as a reliable gate dielectric for transparent TFTs.[5,24]

In order to enhance the dielectric performances of RT-deposited BST thin films, research efforts into the metal (e.g., Mn, Ni, or Mg) doping of a BST host have been made.[5,25–27] Recently, Kim *et al.*[5] reported the successful integration of 1% Ni-doped BST as a gate dielectric for the fabrication of ZnO-TFTs exhibiting a very low operation voltage (4 V), field effect mobility (2.2 $cm^2/V\,s$), current on/off ratio (1.2×10^6), and subthreshold swing (0.21 V/dec). Pentacene-TFTs with 3% Mn-doped BST showed a field effect mobility of 0.32 $cm^2/V\,s$ and a low operating voltage of less than 7 V.[25] Kang *et al.*[27] suggested the potential suitability of a 3% Mg-doped BST gate insulator for high field effect mobility (16.3 $cm^2/V\,s$) TFTs fabricated on PET substrate. All these results are meaningful insofar as they represent the first achievement of low voltage operating ZnO and polymer TFTs with RT-deposited BST gate dielectrics using metal doping. Although there have been a few earlier reports on the material properties of Ni- or Mn-doped BST,[26,28] there have been no in-depth studies on the electronic band structures of TM-doped BST thin films that can provide direct evidence of the electrical enhancements that result from TM doping of BST. There are numerous previous analyses on charge transport in BST thin films with various electrical measurements of metal-insulator-metal (MIM) capacitor configurations,[29–34] wherein several plausible charge transport models including the Schottky emission,[29,30] Fowler–Nordheim (FN),[31,32] and Pool–Frenkel (PF)[33,34] models have been proposed. Nonetheless, the most reliable method is to consider the charge transport model obtained by direct investigation of the electronic band edge structures of BST, which govern the charge injection and transport in BST. It is important to note that systematic spectroscopic studies on the electronic band edge structures of undoped and doped BST are relatively rare. A crucial issue for the experimental study of the electronic band edge states of BST is the detection of defects. Previously published studies have suggested that the oxygen vacancy defects distributed within BST films play a major role in their high leakage currents and charge trapping tendencies.[1,2,34,35] Therefore, an in-depth report on the direct spectroscopic detection of defect states in undoped and TM-doped BST is very desirable for the extended application of BST-related materials.

In this study, various spectroscopic measurements using high resolution rotating compensator enhanced spectroscopic ellipsometry (SE), synchrotron x-ray absorption spectroscopy (XAS), and x-ray photoelectron spectroscopy (XPS) were carried out to probe the band edge states of undoped and Ni-doped BST thin films. Based on the band electronic diagram constructed from the spectroscopic results, we proved the correlation between the changes in defect states in Ni-doped BST and leakage current suppression. SE measurements identify the defect states (i.e., oxygen vacancy states) in the conduction band (CB) edges and, therefore, provide specific information about the change in the defect energy state and density. Furthermore, a physical model of the Ni-doping effect for local structures more symmetrical than undoped BST is proposed, and this model can be largely extended to the explanation of other TM-doped perovskite type ABO_3 thin films.

II. EXPERIMENTAL

Disk-type undoped and 1% Ni-doped BST targets with diameters of 2 in. were prepared by a conventional mixed oxide process. 200 nm thick BST and 1% Ni-doped BST thin films were deposited directly onto Pt (150 nm)/Ti (50 nm)/SiO_2/Si substrates at RT by rf magnetron sputtering under the following operating conditions: an electric power of 80 W, a working pressure of 50 mTorr, and an Ar/O_2 (1/1) atmosphere. For both as-deposited undoped and Ni-doped BST thin films, the stoichiometry of thin films taken by XPS measurements was $-Ba_{0.6}Sr_{0.4}TiO_3$. In order to get the stoichiometry, we calculated the ratio of the XPS peak area of each element over the total XPS area considering the XPS peak sensitivity factor. Regarding Ni-doping concentration, ~1% Ni-doping concentration was estimated based on the combined analyses of energy dispersion spectroscopy and XPS on the disk-type sputtering target and BST thin films.

For electrical measurements, Pt top electrodes (area=4×10^{-4} cm^2) of 100 nm thickness were deposited through a shadow mask using a dc magnetron sputtering system. Leakage J-V characteristics were obtained with a semiconductor parameter analyzer (HP4155A). The dielectric constants were obtained from capacitance-voltage measurements at 1 MHz using an HP4192A impedance analyzer; the relative dielectric constants, k, were 28 for undoped BST films and 26 for Ni-doped BST films. These smaller dielectric constants compared with regular perovskite BST are due to the small grain size in Ni-doped and undoped BST films deposited at RT.

The various spectroscopic measurements of as-deposited films present an opportunity to identify local bonding changes responsible for differences in J-V characteristics between undoped and Ni-doped BST. The real and imaginary parts of the complex dielectric constant, $\varepsilon_c=\varepsilon_1+i\varepsilon_2$, for undoped BST and Ni-doped BST were determined by visible- and vacuum-ultraviolet SEs in a rotating compensator configuration spectrometer.[36] XAS measurements were performed at the Stanford Synchrotron Radiation Laboratories (SSRL) at the Stanford Linear Accelerator Center (SLAC) using the total photoelectron yield to determine the relative absorption strength of the spectral features associated with transitions from TM and O-atom core level states to empty CB states.[37] XPS was carried out to probe the band edge states of undoped and Ni-doped BST thin films using a VG Scientific Escalab 220i-XL spectrometer with a monochromatic Al Kα radiation source.

III. RESULTS AND DISCUSSION

Figures 1(a)–1(c) compares log current density (J)-electric field (E) curves [direct tunneling (DT) plot], log $J\text{-}E^{1/2}$ curves (Schottky plot), and log $(J/E^2)\text{-}1/E$ curves (FN tunneling plot) of MIM capacitors with as-deposited BST and Ni-doped BST dielectrics with top and bottom Pt

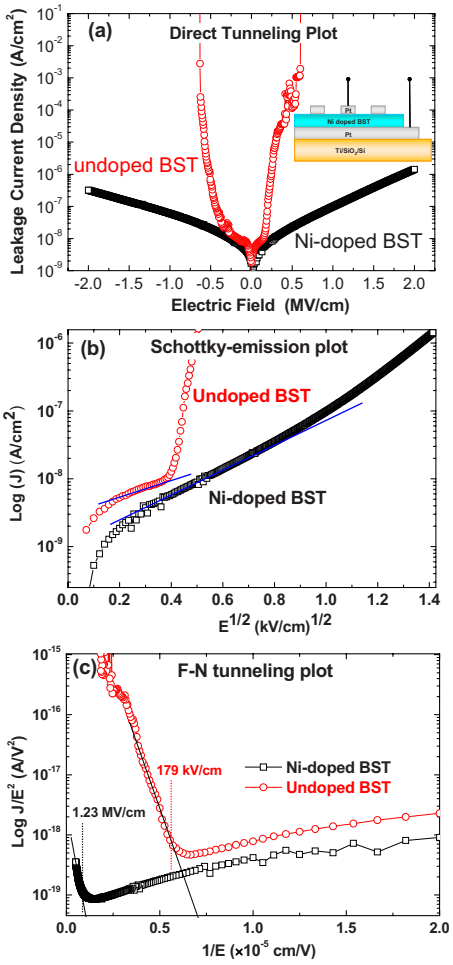

FIG. 1. (Color online) (a) log J vs E (DT plot), (b) log J vs $E^{1/2}$ (Schottky emission plot), and (c) $\log(J/E^2)$ vs 1/E (FN tunneling plot) of Ni-doped and undoped BST MIM cells at RT. A schematic cross-sectional view of a Pt-200 nm Ni/doped BST (or undoped BST)/Pt MIM cell fabricated on a $Ti/SiO_2/Si$ template is shown in the inset of (a). Traces are included for both positive and negative electric fields in a spectral range from −2 to +2 MV/cm. Note that Ni-doped BST shows the clear linearity of the log J-E curve in the D-T plot, but that both the Ni-doped and undoped BST show weak linearity in the Schottky emission plot. At the higher E-field, the linearity of the log J-1/E curve in the FN plot is observed in both the Ni-doped and undoped BST.

electrodes. The applied electric field was swept to ±2 MV/cm (i.e., ±40 V of gate bias) to determine the relative stability of Ni-doped BST under a relatively high electric field and also to reveal any asymmetry in the J-E characteristics. The log J-E curves in Fig. 1(a) show markedly different behaviors with and without Ni-doping in the BST. Asymmetries in J-V plots for undoped BST devices have been assumed to be related to differences in native defects at the top and bottom interfaces consistent with anticipated differences in interface bonding between (i) Pt bottom electrode and the as-deposited BST, and (ii) the surface of the as-deposited BST and the as-deposited Pt top electrode. These differences in the interfaces with native defects depending on either top or bottom Pt electrode are considered as the main reason for the multiple random dielectric breakdowns observed clearly in the positive bias but not in negative bias. Our focus will be on positive gate bias results. For a positive applied bias to the top electrode, the undoped BST displays a rapid increase in current at ~0.1–0.15 MV/cm and multiple *random* dielectric breakdowns at applied voltages >0.7 MV/cm. However, the Ni-doped BST films show no significant increases in J for applied E up to 2 MV/cm in contrast to the rapid J increase in the undoped BST, resulting in two order low J level at an applied voltage of 0.25 MV/cm against the J level of the undoped BST at the same E. The overall aspect of the greatly suppressed leakage current in Ni-doped BST is very similar to that in other previous reports.[25–27]

To investigate the transport mechanism, the Schottky plots of log (J) against $E^{1/2}$ and of the FN tunneling plot of $\log(J/E^2)$ against 1/E were drawn and are shown in Figs. 1(b) and 1(c), respectively. In Fig. 1(b), the linearity in both the plot for the undoped BST and the plot for the Ni-doped BST is weakly observed at the moderate E level, but it is shown in the very limited E regions for both the BST films. One of prevailing arguments regarding the charge injection mechanism is that the polarity-asymmetric J-V characteristics of BST MIM capacitors are mainly due to the Schottky injection mechanism.[34] This is acceptable in part since the asymmetric J-V reflects different metal-oxide interface properties depending on electrodes, as stated above. On the other hand, it is highly possible that oxygen vacancy defects differently distributed at the interfaces impact the injection and transport as well before the FN regime. The defects present in BST thin films (i) contribute the charge carriers as native donors to CB, (ii) cause the change in the energy barrier heights at the metal-oxide interfaces, and (iii) create the defect-assisted transport pathways proposed in trap-assisted tunneling (TAT) or PF.[33] Although the thermal dependence of J-V plots offers supporting evidence for a transport mechanism ruled by either Schottky emission, TAT, FP, or a combination of those, in this study, the correlation of spectroscopically resolved trap energy levels and densities of defects to the charge injection reveals that there should be a more delicate interpretation based on the generalized injection law under defect-controlled tunneling rather than the simple Schottky emission. For Ni-doped BST, in contrast to the Schottky plot, the DT plot of log (J) against E in Fig. 1(a) shows very good linearity over the whole electric field range and reveals the much more symmetric bias polarity dependence of the leakage current.

The FN plot in Fig. 1(c) shows the clear dependence of the charge injection under FN for the high electric field regime. Ni-doped BST showed a significant increase in the threshold electric field of FN to 1.23 MV/cm compared to 179 kV/cm for undoped BST. Such remarkable differences in J-V characteristics for undoped and Ni-doped BST suggest many interesting features in the injection mechanism of Ni-doped BST.

From the collected results on leakage current characteristics discussed above, it is very important to take the oxygen vacancy defects into account when investigating the qualitative differences between the charge injection mechanism and the Schottky injection mechanism. However, there has been no report on the direct evaluation of defect energy states and density in BST using proper techniques other than indirect electrical measurements. In this study, differences between the CB edge defect states of undoped and Ni-doped BST

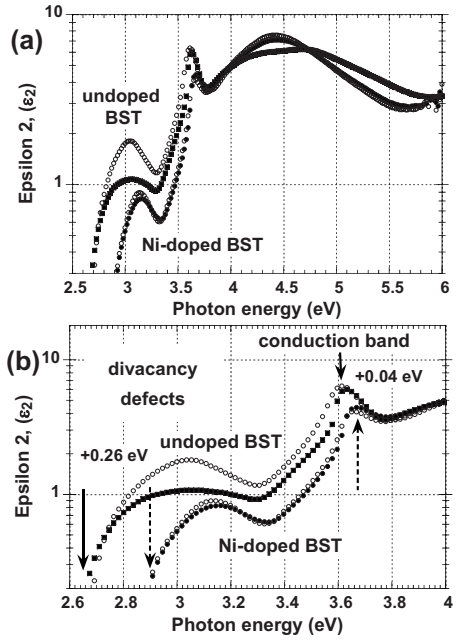

FIG. 2. Epsilon 2 (ε_2) spectra extracted from the SE measurements of undoped and Ni-doped BST. (a) The solid circle points are as-deposited films (RT), and the open circles films are annealed in Ar at 800 °C. (b) ε_2 for as-deposited undoped and Ni-doped BST in a narrower spectral regime from 2.6 to 4.0 eV. This regime emphasizes changes in the spectral character of the band edge defect states. Note that the CB edge states of Ni-doped BST do not change with annealing, while undoped BST shows an increased peak intensity of defect states at around 3 eV.

have been determined *directly* by visible and VUV SE spectroscopy rather than by *indirect extraction* of defect state properties from modeling the temperature dependence of J-V measurements.[35,38,39]

Figure 2(a) presents the spectral dependence of the imaginary part of the complex dielectric constant, ε_2, for undoped and Ni-doped BST, including traces for as-deposited films and for films annealed at 800 °C. Although the main interest of Ni-doped BST thin film in this study is about the RT device application, it is very worthwhile to investigate the annealed undoped and Ni-doped BST thin films focusing the thermally driven (i) local structure distortion under the grain growth or further crystallization and (ii) local grain boundary defect (oxygen vacancy) sites because they provides more useful evidences for Ni-doping effect to the local bonding structures. In Fig. 2(a), the Ni-doped and undoped BST samples display a strong absorption threshold at ~3.3 eV associated with band gap transitions from occupied O-atom nonbonding 2p π states at the top of the valence band (VB) to the lowest empty Ti^{4+} 3d states. These assignments of energy states in the ε_2 spectra are based on a local molecular orbital description, and energy states in the CB between 3.3 and 6 eV are assigned as Jahn–Teller term-split Ti 3d states with a t_{2g} symmetry in the distorted octahedral Ti–O local structure.[40] The relatively broad and weaker ε_2 features between 2.8 and 3.2 eV in the undoped BST spectra are due to intra-d state transitions at native defects. These ε_2 features are due to the transition in the defect levels between *occupied* Ti^{3+} nonbonding e_g states near the VB edge and *empty* antibonding t_{2g} states in the upper half of the band gap of the BST.[40,41] These states are assigned to O-atom defects and are consistent with O-deficient Ti–O bonding with a Ti_2O_3 stoichiometry and are clustered at grain boundaries in nanocrystalline TM oxides.[42] Therefore, it is evident from SE analysis that RT-deposited BST has a distorted octahedral Ti–O local structure. Furthermore, the clearly resolved defect states (Ti^{3+} or oxygen vacancies) in ε_2 spectra reveal the spectral features of defects localized at grain boundaries rather than the randomly distributed defects in the unit cells of a single crystalline oxide.[43] However, the prevalent techniques such as x-ray diffraction and high resolution transmission electron microscope did not clearly reveal the nanocrystallinity of RT-deposited BST (not shown here) because these techniques are limited to identifying lengths less than 3–4 nm in the as-deposited TM oxides.[43] Therefore, it is uncertain whether RT-deposited BST should be declared nanocrystalline or amorphous. However, in this study, RT-deposited BST is defined as a nanocrystalline material because spectroscopic results clearly support the distorted octahedral Ti–O structures and localized defects with a detection of corresponding band edge changes. A strictly defined amorphous structure should reveal the sort of completely random disorder found in amorphous SiO_2, and, in fact, there is an interesting report on SiO_2-like amorphous structure thermally stable up to 1000 °C in the pseudoternary transition complex metal oxide alloy $(TiO_2)_x(SiO_2)_y(Si_3N_4)_{1-x-y}$ $(x, y < 1)$, which has a tetrahedral (fourfold) Ti–O configuration rather than an octahedral (sixfold) Ti–O configuration.[44]

Figure 2(b) indicates the spectral dependence of ε_2 for BST and Ni-doped BST in a more limited spectral regime from 2.6 to 4 eV to highlight a difference in photon energy of $\sim 0.26 \pm 0.15$ eV between the threshold for trapping in undoped BST, ~2.65 eV, and Ni-doped BST, ~2.91 eV.

The resonance energies of the Ti 3d state features in the as-deposited films have been obtained by differentiation of the respective ε_2 spectra[40] and are displayed in Fig. 3(a). Based on spectroscopic studies of band edge states in TiO_2, spectrum features at photon energies >3.3 eV are assigned to Ti^{4+} t_{2g} empty CB states and features below 3.5 eV to Ti^{3+} band edge defects.[40,41] The threefold degeneracy of the t_{2g} states is removed in undoped BST, indicating a distorted octahedral bonding environment between Ti and its six O-atom neighbors, e.g., an orthorhombic unit cell structure with different distortions in the x, y, and z directions, as indicated in Fig. 3(b). Band edge defects are assigned to Ti^{3+} bonding that is compensated by O-atom vacancy defects clustered at grain boundaries.[40] Transitions giving rise to defect features are from occupied Ti^{3+} e_g occupied d states at the VB edge to unoccupied Ti^{3+} t_{2g} d states at the CB edge.[45] There are also two weaker features in the derivative spectra at 4.0 eV in the Ti^{4+} t_{2g} region of the spectrum and ~2.80 eV in the Ti^{3+} t_{2g} region of the defect states.

Figure 3(a) identifies a significant difference between the Ti t_{2g} empty states in undoped and Ni-doped BST. As noted above, the threefold degeneracy of the Ti 3d t_{2g} state is completely removed in the undoped BST, while the degeneracy is only partially removed in the Ni-doped BST. The partial removal is consistent with a change in the local bonding geometry at the Ti^{4+} sites from either orthorhombic or monoclinic Ti–O local structures in the undoped BST to tetragonal

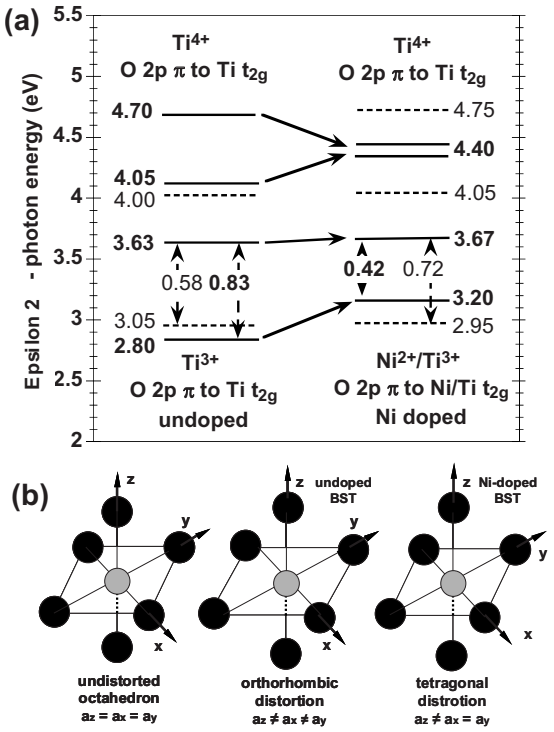

FIG. 3. (a) Schematic energy band diagram for CB empty antibonding states, and band edge defects states for undoped and Ni-doped BST obtained from analysis of ε_2 spectra. Solid lines indicate boldface energy level positions, and energy differences reflect strong features in the ε_2 spectra, whereas dashed lines and plain text indicate significantly weaker spectral features. (b) Local bonding of Ti atoms (gray) and O atoms (black) in (i) undistorted octahedral arrangements in which all bond lengths, a_x, a_y, and a_z are equal, (ii) orthorhombic arrangements in which all bond lengths are unequal, and (iii) in tetragonal arrangements with two equal bond lengths.

Ti–O local structures in the Ni-doped BST.[45] Based on the twofold degeneracy of the higher-lying t_{2g} state in Ni-doped BST, the centroids of the t_{2g} states in undoped and Ni-doped BST are effectively the same, and equal to 4.15 ± 0.15 eV, consistent with the sixfold coordination of Ti by O-atom neighbors.

Figure 3(a) also summarizes differences in spectroscopic features attributed to band edge O-atom vacancies for undoped and Ni-doped BST. The basis for these assignments derives from previously published studies of TiO_2 band edge intrinsic defects attributed to Ti^{3+} bonding in divacancy defects clustered at grain boundaries between nanograins.[40] There are several important properties of these band edge defects in the energy range from 2.6 to 3.3 eV: (i) the thresholds for absorption into empty defects are (a) independent of the processing temperature in the Ni-doped BST and (b) there is increased absorption in the annealed undoped BST at 800 °C, but not in the Ni-doped BST, and most importantly, (ii) the threshold for absorption in the Ni-doped BST is upshifted by 0.26 eV; i.e., it is closer to the CB edge in Ni-doped BST. This change in the defect state energy in Ni-doped BST correlates with the change in symmetry of the Ti atom empty t_{2g} states, showing that the energy shift is the same as the average of the combined shifts for the change from the two higher-lying t_{2g} states in undoped BST to a single state in Ni-doped BST.

The changes in the band edge defects are consistent with

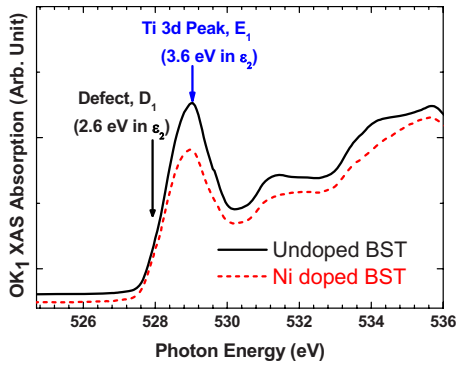

FIG. 4. (Color online) XAS OK_1 edge spectra of Ni-doped and undoped BST. The weak state at 528 eV (D_1) corresponds to the defect state at 2.6 eV in the ε_2 spectra, but the energy is not clearly resolved in the spectra with the limited spectral resolution. The strong peak at 529 eV (E_1) corresponds to the Ti 3d state peak at 3.6 eV in the ε_2 spectra, and the relative peak strength between the Ni-doped and undoped BST is similar to the ε_2 spectra. The overall Ti 3d state features of undoped BST up to 533 eV are more distinctive than Ni-doped BST, meaning that the features in the ε_2 spectra are associated with the intrinsic CB states.

the substitution of divalent Ni^{2+} for tetravalent Ti^{4+}. To maintain local charge neutrality, the divalent Ni^{2+} atoms must be part of the divacancy structure, so that it can no longer be characterized as a Ti^{3+} defect but rather must be characterized as a divacancy that includes both Ni^{2+} and Ti^{3+} atomic species.[42] The correlated spectral changes in both the empty t_{2g} states and the band edge defect suggest that the change in symmetry for the Ti^{4+} atoms is driven by an effect associated with the local dipoles at the divacancies, which include a significant dipole concentration for the Ni^{2+} bonding state.[42] More importantly, if considering oxygen vacancies or Ti^{3+} states at the CB edge, it is clear that Ni doping reduces the density of pre-existing defects in the bulk BST, as shown in Fig. 2(a). The physical defect density in the ε_2 spectra can be estimated by the f-sum rule, wherein the density of states is calculated from absorption by taking the matrix enhancements for each band into account for the relative strength of the absorption coefficient,[40,46] and this yields about 1.9×10^{18} cm^{-3} for the Ni-doped BST which is reduced by an order magnitude from the defect density in undoped BST at 1.3×10^{19}. This value is similar to the defect density in Mn-doped BST estimated from the defect chemistry calculation,[47] but it should be pointed out that the density value in this study is estimated from the directly measured data.

Figure 4 displays the OK_1 XAS spectra for Ni-doped and undoped BST. These XAS spectra show the CB states in the more extended energy range and confirm the CB states assigned in the ε_2 spectra of Fig. 2(a). The sharpest primary peak states (E_1) at 529 eV for both the Ni-doped and undoped BST correspond to the Ti^{4+} 3d states at 3.6 eV in the ε_2 spectra. The relative strength of peaks at 529 eV between the Ni-doped and undoped BST also agrees with that of Ti^{4+} 2g peaks at 3.6 eV in the ε_2 spectra. The OK_1 XAS spectra resolution is insufficient for the clear energy position assignments of each peak state for both BSTs. However, observations of the overall spectral features of the Ti 3d states that exist up to about 533 eV indicate that undoped BST has the

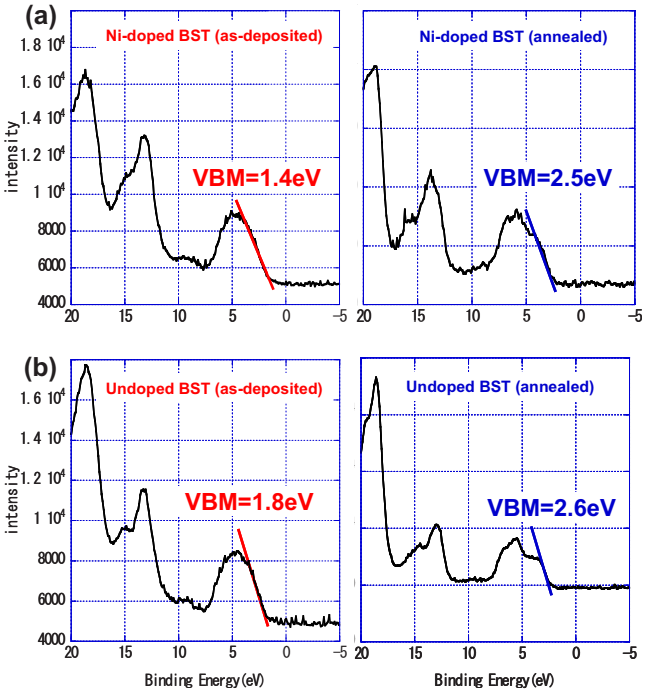

FIG. 5. (Color online) XPS spectra of the VB edge of (a) as-deposited and annealed Ni-doped BST and (b) as-deposited and annealed undoped BST. The E_F level corresponds to 0 eV of binding energy. The VB maximum (VBM) energy level for each film is achieved by the linear extrapolation of the strong onset of the VB edge. The E_F level of the as-deposited Ni-doped BST is 0.4 eV lower than that of the undoped BST with respect to VBM, but the difference of E_F levels between the doped and undoped BST becomes smaller at 0.1 eV with annealing at 800 °C.

more distinctive CB state term splitting in the spectra compared to Ni-doped BST. This is because undoped BST suffers from the asymmetric distortion of its Ti–O octahedron while the Ti–O octahedron in Ni-doped BST is partly stabilized to a more symmetric local structure, as shown in Figs. 3(a) and 3(b). Therefore, these OK_1 XAS spectra reinforce the CB edge Ti 3d state and the defect state assignments in the ε_2 spectra shown in Fig. 2(a).

In addition to the analysis of CB state changes, it is important to investigate the effect of Ni doping on the Fermi level (E_F) to understand the charge injection mechanism. This can be studied through VB edge XPS analysis, as shown in Fig. 5. Because the RT-deposited BST with the short nanocrystallites less than 4 nm is qualitatively different from the long-range ordered BST (i.e., regular perovskite $Ba_{0.6}Sr_{0.4}TiO_3$ having paraelectricity[48]) annealed at the high temperature, both the as-deposited sample and the sample annealed at 800 °C were measured by XPS for comparison. It is noted that the E_F level of the annealed Ni-doped BST (2.5 eV above VB edge) and that of the undoped BST (2.6 eV above VB edge) are comparable to the reported value (2.9 eV above VB edge for the undoped BST) in Ref. 49. In contrast, the as-deposited BST samples showed much deeper E_F levels in the energy gap than the annealed samples, which registered 1.4 eV for the Ni-doped BST and 1.8 eV for the undoped BST above the VB edge, respectively. Therefore, Ni doping of BST lowered the E_F level toward the VB edge by 0.4 eV from that of the undoped BST. For another comparison, the XPS results for the Mn-doped BST in Ref. 47

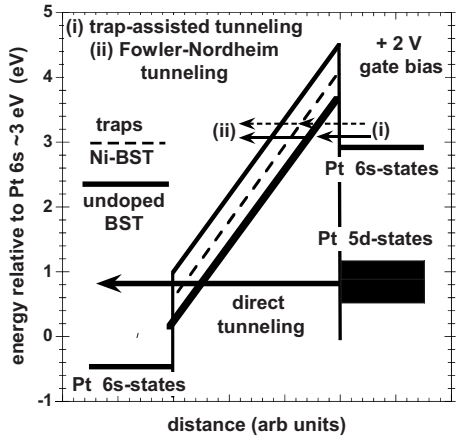

FIG. 6. Band alignment for the band edge defects in undoped (heavy solid line) and Ni-doped (dashed line) BST MIM capacitors. The Pt 6s state indicates the metal gate Fermi levels and the Pt 5d state indicates the filled band. Transport processes are indicated by arrows beginning in the Pt electrodes of the cathode (negative) and are differentiated by the character of these arrows.

showed that the E_F level was lowered through Mn doping by 0.7 eV, and, therefore, was placed at 2.2 eV above the VB edge.

Consequently, the change in E_F with Ni doping evidently affects the interfacial barrier heights. Dawber *et al.*[49] reported a good approximation for the Schottky barrier heights with charge neutral levels affected by E_F and the energy distribution of surface states. It is interesting to note that the differences in the energy and density of Ti^{3+} defect states between the Ni-doped and undoped BSTs observed in the ε_2 spectra might be the other replication of E_F level changes. In order words, the relatively higher density of empty Ti^{3+} defect states in undoped BST than the Ni^{2+}/Ti^{3+} defect states in Ni-doped BST results in an E_F level 0.4 eV closer to the CB edge, indicating more n-type characteristics than are present in Ni-doped BST. Therefore, it can be equivalently stated that Ni doping causes acceptorlike effects for BST.[26] However, it is noted that the E_F level shift with Ni doping is relatively small compared to that with Mn doping reported in Ref. 49.

Figure 6 is an interfacial band alignment diagram in which (i) the BST-Pt CB energy difference is 1.4 eV, which is estimated from the relative E_F position of the undoped BST with respect to the E_F (2.9 eV) of the BST corresponding to the barrier heights (~0.6 eV) in other reports;[50,51] (ii) the trap depth for the undoped and Ni-doped BSTs are indicated, respectively, by the solid and dashed lines; and (iii) three tunneling pathways are indicated: (a) FN and (b) TAT for the undoped BST by the solid arrows, and (c) a DT mechanism for the Ni-doped BST in which the electrons are supplied from occupied Pt 5d states.[35,52]

The relative trap depths and the lower density of the traps in the Ni-doped BST compared to those of the undoped BST are consistent with the following assignments: (i) the TAT/FN tunneling is responsible for the rapid rise in current for the undoped BST MIM with an electric field of 179 kV/cm;[46] (ii) the reduced trap density and position of the trap in the biased MIM do not support a TAT/FN tunneling pro-

cess for MIMs with Ni-doped BST, so instead, a symmetric DT mechanism prevails; and (iii) the asymmetry between + and − gate biases is due to differences in interfacial bonding for the deposition of BST on Pt and the deposition of Pt on BST. These results suggest an approach to improve RT-deposited BST for a gate dielectric application in transparent TFTs that is based on the changes in defect state energies and densities between undoped and Ni-doped BST.

Based on the Schottky emission theory, the excellent leakage suppression with Ni doping is not well explained by the small barrier difference between Ni-doped and undoped BST in this study. In particular, the very symmetric J-V curve of Ni-doped BST is not the typical characteristic of a Schottky emission, and furthermore, the DT plot of Ni-doped BST in Fig. 1(a) shows the linearity of the log J-E curve. Therefore, the tunneling scheme proposed in Fig. 6 can offer a more plausible model to explain the J-E characteristics based on the combined spectroscopic results.

IV. CONCLUSIONS

In conclusion, the transition from direct to trap-assisted/FN tunneling in MIM capacitors is suppressed when Ni-doped BST thin film dielectrics are substituted for undoped BST. For Ni doping at the one percent level, the spectral dependences of (i) the imaginary part of the complex dielectric constant, ε_2, obtained from SE, (ii) the OK_1 edge XAS spectra, and (iii) the VB edge XPS spectra show significant differences in the band edge trap depth relative to undoped BST. The different trap energies and densities are due to the partially symmetric structures (tetragonal) of the Ti–O local structure in BST with Ni doping, as confirmed in CF splitting. It was found that these changes in defect state energies relative to the CB edge are directly responsible for the improved electrical performance in MIM capacitors with the Ni-doped BST dielectrics. Thus, these results provide a possible approach for both the analysis and processing of defect control in RT-deposited BST with TM doping for low temperature applications such as TFT gate dielectrics.

[1]A. I. Kingon, J. P. Maria, and S. K. Streiffer, Nature (London) **406**, 1032 (2000).
[2]N. Konofaos, E. K. Evangelou, Z. Wang, and U. Helmersson, IEEE Trans. Electron Devices **51**, 1202 (2004).
[3]K. Yamabe, M. Inomoto, and K. Imami, Jpn. J. Appl. Phys., Part 2 **37**, L1162 (1998).
[4]E. Y. Wu and J. H. Stathis, and L. K. Han, Semicond. Sci. Technol. **15**, 425 (2000).
[5]Y. B. Kim, J. U. Kim, D. K. Choi, J. M. Hong, and I. D. Kim, J. Electroceram. **23**, 76 (2008).
[6]C. D. Dimitrakopoulos, S. Purushothaman, J. Kymissis, A. Callegari, and J. M. Shaw, Science **283**, 822 (1999).
[7]K. Nomura, H. Ohta, K. Ueda, T. Kamiya, M. Hirano, and H. Hosono, Science **300**, 1269 (2003).
[8]Y. Kwon, Y. Li, Y. W. Heo, M. Jones, P. H. Holloway, D. P. Norton, Z. V. Park, and S. Li, Appl. Phys. Lett. **84**, 2685 (2004).
[9]P. F. Carcia, R. S. McLean, and M. H. Reilly, Appl. Phys. Lett. **88**, 123509 (2006).
[10]L. A. Majewski, R. Schroeder, and M. Grell, Adv. Mater. (Weinheim, Ger.) **17**, 192 (2005).
[11]Y. W. Choi, I. D. Kim, H. L. Tuller, and A. I. Akinwande, IEEE Trans. Electron Devices **52**, 2819 (2005).
[12]Th. B. Singh, N. Marjanovic, P. Stadler, M. Auinger, G. J. Matt, S. Günes, N. S. Sariciftci, R. Schwödiauer, and S. Bauer, J. Appl. Phys. **97**, 083714 (2005).
[13]H. S. P. Wong, IBM J. Res. Dev. **46**, 133 (2002).
[14]D. W. Greve, *Field-Effect Devices and Applications* (Prentice-Hall, Englewood Cliffs, NJ, 1998).
[15]N. Heberkorn and J. Guimpel, Appl. Phys. Lett. **87**, 042509 (2005).
[16]M. Sedlar and M. Sayer, Integr. Ferroelectr. **10**, 113 (1995).
[17]D. Y. Noh, H. H. Lee, T. S. Kang, and J. H. Je, Appl. Phys. Lett. **72**, 2823 (1998).
[18]S. Paek, J. Won, K. Lee, J. Choi, and C. Park, Jpn. J. Appl. Phys., Part 1 **35**, 5757 (1996).
[19]K. H. Lee, C. S. Hwang, B. T. Lee, W. D. Kim, H. Horii, C. S. Kang, H. J. Cho, S. I. Lee, and M. Y. Lee, Jpn. J. Appl. Phys., Part 1 **36**, 5860 (1997).
[20]T. Horikawa, T. Makita, T. Kuroiwa, and N. Mikami, Jpn. J. Appl. Phys., Part 1 **34**, 5478 (1995).
[21]Y. Fukuda, K. Numata, K. Aoki, and A. Nishimura, Jpn. J. Appl. Phys., Part 1 **35**, 5178 (1996).
[22]S. Yamamichi, A. Yamamichi, D. Park, and C. Hu, Tech. Dig. - Int. Electron Devices Meet. **1997**, 261.
[23]A. Martin, P. O'Sullivan, and A. Mathewson, Microelectron. Reliab. **38**, 37 (1998).
[24]W. J. Lee, I. K. Park, G. E. Jiang, and H. G. Kim, Jpn. J. Appl. Phys., Part 1 **34**, 196 (1995).
[25]K. T. Kang, M. H. Lim, H. G. Kim, Y. Choi, H. L. Tuller, I. D. Kim, and J. H. Hong, Appl. Phys. Lett. **87**, 242908 (2005).
[26]K. Ahn, S. Baik, and S. S. Kim, J. Appl. Phys. **92**, 2651 (2002).
[27]K. T. Kang, M. H. Lim, H. G. Kim, I. D. Kim, and J. M. Hong, Appl. Phys. Lett. **90**, 043502 (2007).
[28]M. H. Lim, H. S. Kim, N. Y. Kim, H. G. Kim, I. D. Kim, S. E. Moon, M. H. Kwak, H. C. Ryu, and S. J. Lee, J. Electroceram. **13**, 239 (2004).
[29]G. W. Dietz and R. Waser, Thin Solid Films **299**, 53 (1997).
[30]J. F. Scott, Ferroelectrics **232**, 25 (1999).
[31]I. Stolichnov and A. K. Tagantsev, J. Appl. Phys. **84**, 3216 (1998).
[32]K. C. Kao and W. Hwang, *Electrical Transport in Solids* (Pergamon, London, 1981).
[33]J. Frenkel, Phys. Rev. **54**, 647 (1938).
[34]M. Dawber, K. M. Rabe, and J. F. Scott, Rev. Mod. Phys. **77**, 1083 (2005).
[35]R. Waser, J. Am. Ceram. Soc. **74**, 1934 (1991).
[36]T. Mori and D. E. Aspnes, Thin Solid Films **455–456**, 33 (2004).
[37]G. Lucovsky, J. G. Hong, C. C. Fulton, Y. Zou, R. J. Nemanich, and H. Ade, J. Vac. Sci. Technol. B **22**, 2132 (2004).
[38]K. Abe and S. Komatsu, Jpn. J. Appl. Phys., Part 2 **31**, 2985 (1992).
[39]G. Ribes, S. Bruyère, D. Roy, C. Parthasarthy, M. Müller, M. Denais, V. Huard, T. Skotnicki, and G. Ghibaudo, IEEE Trans. Device Mater. Reliab. **6**, 132 (2006).
[40]G. Lucovsky, H. Seo, S. Lee, L. B. Fleming, M. D. Ulrich, J. Lüning, P. Lysaght, and G. Bersuker, Jpn. J. Appl. Phys., Part 1 **46**, 1899 (2007).
[41]L. Fleming, C. C. Fulton, G. Lucovsky, J. E. Rowe, M. D. Ulrich, and J. Lüning, J. Appl. Phys. **102**, 033707 (2007).
[42]W. L. Warren, G. E. Pike, K. Vanheusden, D. Dimos, B. A. Tuttle, and J. Robertson, J. Appl. Phys. **79**, 9250 (1996).
[43]H. Seo, G. Lucovsky, L. B. Fleming, M. D. Ulrich, J. Lüning, G. Koster, and T. H. Geballe, Microelectron. Eng. **84**, 2298 (2007).
[44]H. Seo, S. Lee, B. Ju, G. Lucovsky, and J. Lüning, AIP Conf. Proc. **882**, 487 (2007).
[45]P. A. Cox, *Transition Metal Oxides* (Clarendon, Oxford, 1992), p. 40.
[46]H. R. Philipp and H. Ehrenreich, Phys. Rev. **129**, 1550 (1963).
[47]T. Mihara, H. Watanabe, H. Yoshomori, C. A. Paz Araujo, B. Melnick, and L. D. McMillan, Integr. Ferroelectr. **1**, 269 (1992).
[48]S. Ezhilvalavan and T. Y. Tseng, Mater. Chem. Phys. **65**, 227 (2000).
[49]M. Dawber, J. F. Scott, and A. J. Hartmann, J. Eur. Ceram. Soc. **21**, 1633 (2001).
[50]S. Zafar, R. E. Jones, B. Jiang, B. White, V. Kaushik, and S. Gillespie, Appl. Phys. Lett. **73**, 3533 (1998).
[51]J. F. Scott, Ferroelectr. Rev. **21**, 1 (1998).
[52]M. Depas, B. Vermeire, P. W. Mertens, R. L. Van Meirhaeghe, and M. M. Heyns, Solid-State Electron. **38**, 1465 (1995).